

Convectively Induced Secondary Circulations in Fine-Grid Mesoscale Numerical Weather Prediction Models

J. CHING,* R. ROTUNNO,⁺ M. LEMONE,⁺ A. MARTILLI,[#] B. KOSOVIC,⁺ P. A. JIMENEZ,^{+,#} AND J. DUDHIA⁺

* *Institute for the Environment, University of North Carolina at Chapel Hill, Chapel Hill, North Carolina*

⁺ *National Center for Atmospheric Research, Boulder, Colorado*

[#] *CIEMAT, Madrid, Spain*

(Manuscript received 8 October 2013, in final form 2 May 2014)

ABSTRACT

Mesoscale numerical weather prediction models using fine-grid [$O(1)$ km] meshes for weather forecasting, environmental assessment, and other applications capture aspects of larger-than-grid-mesh size, convectively induced secondary circulations (CISCs) such as cells and rolls that occur in the convective planetary boundary layer (PBL). However, 1-km grid spacing is too large for the simulation of the interaction of CISCs with smaller-scale turbulence. The existence of CISCs also violates the neglect of horizontal gradients of turbulent quantities in current PBL schemes. Both aspects—poorly resolved CISCs and a violation of the assumptions behind PBL schemes—are examples of what occurs in Wyngaard's "terra incognita," where horizontal grid spacing is comparable to the scale of the simulated motions. Thus, model CISCs (M-CISCs) cannot be simulated reliably. This paper describes how the superadiabatic layer in the lower convective PBL together with increased horizontal resolution allow the critical Rayleigh number to be exceeded and thus allow generation of M-CISCs like those in nature; and how the M-CISCs eventually neutralize the virtual temperature stratification, lowering the Rayleigh number and stopping their growth. Two options for removing M-CISCs while retaining their fluxes are 1) introducing nonlocal closure schemes for more effective removal of heat from the surface and 2) restricting the effective Rayleigh number to remain subcritical. It is demonstrated that CISCs are correctly handled by large-eddy simulation (LES) and thus may provide a way to improve representation of them or their effects. For some applications, it may suffice to allow M-CISCs to develop, but account for their shortcomings during interpretation.

1. Introduction

Solar energy received by Earth's atmosphere translates into evolving circulation systems ranging from global to submillimeter scales. Turbulence in this context is made up of random eddy motions generated by wind shear and buoyancy forces, which transport heat, moisture, and trace gases. In the daytime planetary boundary layer (PBL), the largest eddies, which we will call convectively induced secondary circulations [CISCs, the primary circulation being the large-scale atmospheric flow (see definition 3 at http://glossary.ametsoc.org/wiki/Secondary_circulation)], scale with the PBL depth h . Typical daytime h values range from less than 100 m in the early morning to midday values from

~1 km to more than 2 km in fair-weather conditions. Thus, CISCs have a typical horizontal wavelength of the order of 2–10 km. Their presence is revealed in satellite images of low clouds over land and sea (e.g., Fig. 1) and is detected on weather radar scans on a frequent basis.

Now that increased computational capability makes possible running mesoscale models with a horizontal grid spacing of 1 km or less, simulations that include modeled CISCs (M-CISCs) have started to appear in the literature regarding meteorological problems related to flow in cities, effects of heterogeneous terrain or surface properties, hurricane evolution, thunderstorm initiation and propagation, and the dispersion of pollutants. In the dispersion context for example, the desire for such fine resolution is motivated by the fact that pollution sources and thus their concentration fields have a high degree of spatial granularity. Examples of modeling issues of relevance include but are not limited to 1) Does performing air quality modeling at fine scales require modeling of the meteorological fields at commensurate scales, or

Corresponding author address: Jason Ching, Institute for the Environment, 100 Europa Dr., Suite 490, Campus Box 1105, Chapel Hill, NC 27517.
E-mail: jksching@gmail.com

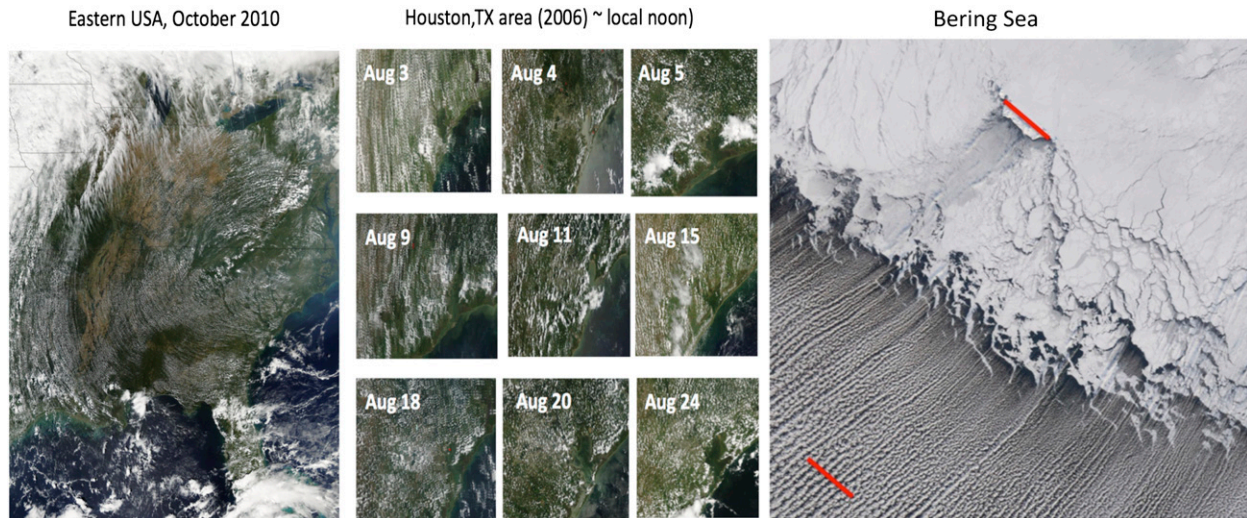


FIG. 1. (left),(middle) Over land convectively generated cloud fields in undisturbed flow conditions from MODIS *Aqua* (ascending) and *Terra* (descending) satellite platforms over eastern United States and Houston, TX, area, respectively. Images are approximately local noon. Data are from online (<http://lance.nasa.gov/imagery/rapid-response>). (right) Over water cloud streets generated as CISCs from outflow off of Iceland over the Bering Sea. St. Matthews Island (52 km long) is denoted with a red line. Another red line of 52 km is translated downwind for scale comparison with roll size.

are interpolated fields adequate? And 2) how accurate or realistic are numerical weather prediction models run at increasingly finer grid meshes?

In the present study, we use the research version of the Weather Research and Forecasting Model (WRF; Skamarock et al. 2008) version 3.2 to explore these questions. Our work is motivated by nested-grid (spacings of 27, 9, 3, and 1 km) simulations of the weather in the Houston–Galveston, Texas, area during the 2006 Texas Air Quality Study (AQS-2006; ESRL 2006); sample results for 4 August 2006 are shown in Fig. 2. These results are part of a study to assess the appropriateness of data from the innermost grid as input for air quality application simulations using the Community Multiscale Air Quality (CMAQ; Byun and Schere 2006) modeling system. Focusing on an $81 \text{ km} \times 81 \text{ km}$ domain over Houston, the 27- and 9-km grid simulations in Fig. 2 show a mean $h(x, y)$ of about 1 km with little if any spatial gradient. More spatial variations in $h(x, y)$ appear at 3 km with several areas of 1.2–1.5-km height; in the 1-km grid simulation, the $h(x, y)$ fields become even more spatially complex and variable with peak values exceeding 1.6 km. The patterns in the 1- and 3-km grid simulations are qualitatively similar in scale and appearance to the satellite-based fields in Fig. 1. LeMone et al. (2010) noted the pattern of model PBL structures strongly resembled satellite cloud-field images, which included rolls, cells, and rolls superposed on apparent wave structures. However, they also found that the horizontal wavelength was reduced and that the M-CISCs became

more cellular and less realistic when the grid spacing was reduced from 1 km to 333 m. Likewise, Bornstein et al. (2012) show M-CISC horizontal size to decrease and horizontal structure to change with smaller grid spacing.

The fidelity of these modeled fine-grid PBL structures is further called into question when simulations using different PBL schemes are examined. Figure 3 shows $w(x, y)$ at $\sim 125 \text{ m}$ AGL at 2000 UTC (1400 CST) for simulations using 1-km grids, for all seven PBL schemes available in WRF version 3.2 along with the Moderate Resolution Imaging Spectroradiometer (MODIS) satellite image for 1720 UTC. Assuming the clouds formed in response to PBL circulations, $w(x, y)$ provides a crude surrogate for the cloud field; we again see that the simulation produces horizontal features with patterns that are similar to the satellite cloud field. However, we also see large differences in the patterns based merely on the PBL scheme.

In summary, while horizontal variations of important PBL parameters resembling the observed PBL-associated cloud features appear at grid sizes of $\sim 1 \text{ km}$, the horizontal variations in modeled fields [such as $h(x, y)$, $w(x, y)$, etc.] are grid-size-dependent and they depend on the PBL scheme. These problems are related to the fact that the simulations presently described use horizontal grid spacings within the range corresponding to Wyngaard's (2004) "terra incognita." As illustrated in Fig. 4, the terra incognita includes horizontal grid sizes that are too small to meet the assumptions implicit in Reynolds-averaged Navier–Stokes (RANS) modeling, yet too large for a large-eddy simulation (LES).

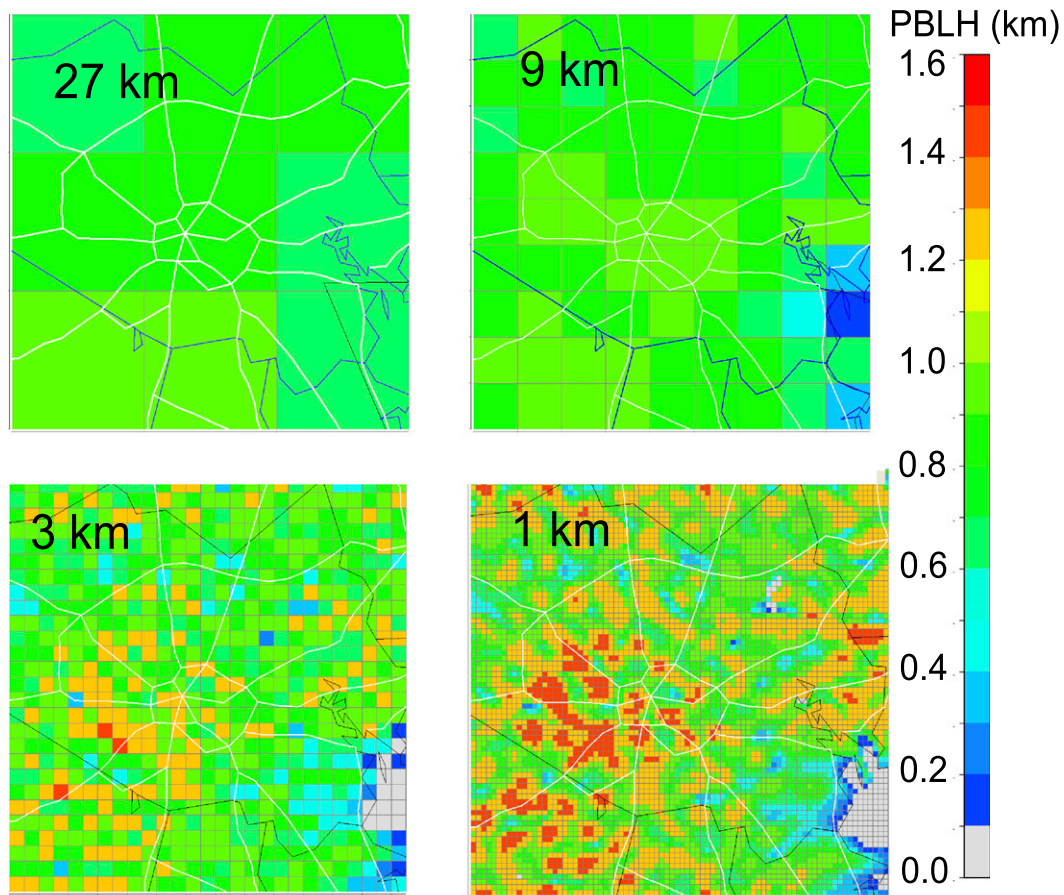


FIG. 2. Nested WRF version 3.2 model simulations of PBL heights for $81 \text{ km} \times 88 \text{ km}$ model domain centered over Houston, for midday, 4 Aug 2006, and for grid resolutions ranging from 27 to 1 km.

In this paper, we explore some of the consequences of mesoscale modeling in the terra incognita. In [section 2](#), we describe the limitations of fine-grid-mesh mesoscale model simulations and look more carefully at observed and modeled CISCs. [Section 3](#) proposes a theoretical explanation for the M-CISCs using the classical linear theory of [Rayleigh \(1916\)](#), discusses progressively more complex idealizations, and ends with a comparison of M-CISC growth rates in a WRF simulation to the theory. [Section 4](#) suggests some strategies for conducting fine-grid simulations that may avoid some of the pitfalls identified here. [Section 5](#) reports on WRF simulations of M-CISCs at a resolution high enough to be in the LES regime. [Section 6](#) contains a summary and outlook.

2. Mesoscale simulations and real and modeled CISCs

In mesoscale simulations, the RANS equations are used to represent the effects of turbulence on time tendencies of heat, momentum, moisture, and other

quantities of interest, such as trace gases. In the typical parameterization, the scales of turbulent motion are presumed to be separated from mesoscale or synoptic-scale motions. Hence, current PBL schemes for RANS-based simulations are based on the assumptions that horizontal gradients of turbulent fluxes are much less than their vertical gradients and thus negligible, and that a grid area is large enough to have many turbulent eddies whose spatially averaged behavior is equivalent to that of a hypothetical ensemble average at a location. Mesoscale models such as WRF using a variety of PBL schemes ([UCAR 2014](#)) have been shown to make reasonably accurate predictions of large to mesoscale weather phenomena down to scales of a few tens of kilometers in the horizontal. This experience is consistent with the expectation that the predicted motions have characteristic scales much larger than the turbulence characteristic scale l in [Fig. 4](#), meaning that a grid mesh size of $\Delta \sim 10 \text{ km}$ is adequate and safely outside of the terra incognita. Of course, 10-km-mesh simulations cannot capture CISCs.

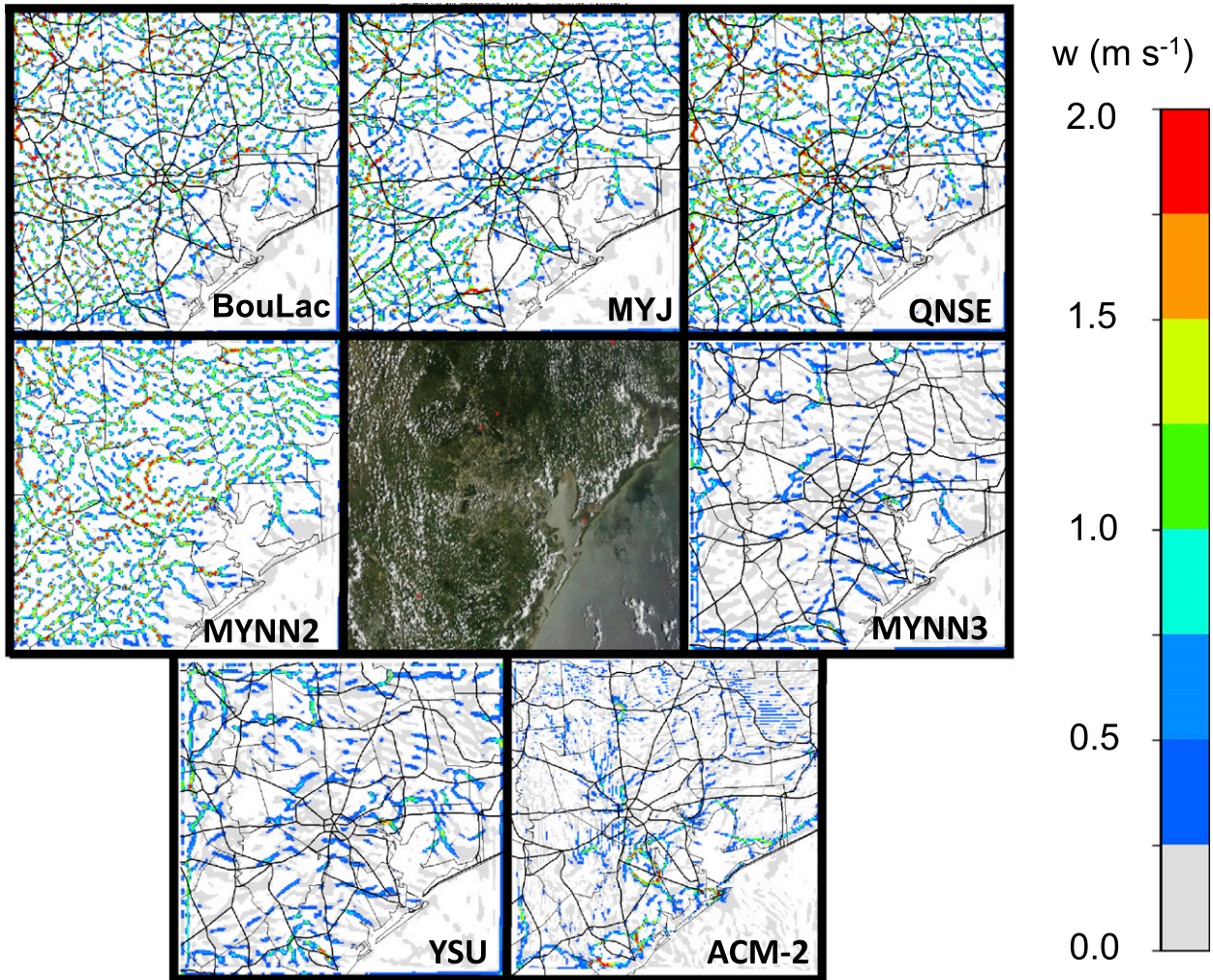


FIG. 3. Comparison of observed PBL-generated clouds to positive vertical velocity (w) at 125 m (level 10) for 2000 UTC 4 Aug 2006 over the Houston–Galveston area using various PBL schemes in WRF at 1-km grid spacing. Satellite image, *Terra*, 1720 UTC, 500-m pixels in center. For the PBL schemes shown, vertical fluxes are proportional to local vertical gradients for BouLac, MYJ, QNSE, and MYNN2; while nonlocal vertical fluxes (independent of local vertical gradients) are also allowed for MYNN3, YSU, and the asymmetric cloud model version 2 (ACM-2).

Before assessing the reality of M-CISCs, it is important to understand observed CISCs. CISCs are long lived ($\tau \gg l/w_*$), where $w_* = [ghT_v^{-1}(\overline{w'T'_v})_0]^{1/3}$, T_v is the virtual temperature, and $gT_v^{-1}(\overline{w'T'_v})_0$ is the surface buoyancy flux. CISCs take the form of cells or horizontal roll vortices depending on the relative strength of buoyancy- and shear-generated energy sources, with rolls (or cells organized in lines) generally occurring for $-25 < h/L < 0$ (Deardorff 1972; LeMone 1973; Grossman 1982; Weckwerth et al. 1997; Young et al. 2002), and more cellular structure for $-h/L \ll 25$ (L is the Obukhov length). Numerous field programs provide evidence for 2D horizontal roll vortices or 3D cellular structure in the daytime fair-weather boundary layer (LeMone 1973; Weckwerth et al. 1997, 1999; Young

et al. 2002; Miao and Chen 2008; LeMone et al. 2010; Xue and Martin 2006).

The appearance of realistic-looking M-CISCs in fair-weather WRF simulations with 1-km grid meshes is related to their horizontal scale of 1–10 km being approximately $(1-10)h$. In such situations, since the turbulence integral scale $\sim h \sim l \sim 1$ km, the grid size lies within the terra incognita (Fig. 4). As a consequence, PBL parameterizations produce ensemble-mean fluxes by subgrid-scale motions that in principle include scales of the same order as the M-CISCs—in strong violation of the assumption that the boundary layer is horizontally homogeneous.

In spite of this violation, M-CISCs behave in a qualitatively realistic way. For example M-CISCs modulate

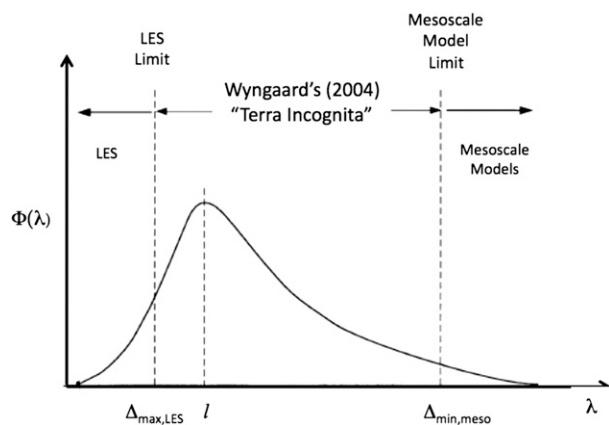


FIG. 4. Schematic energy spectrum showing the spatial regimes including the terra incognita for grid sizes Δ in mesoscale and LES models relative to turbulent eddy structures with peak eddy size represented by l .

the turbulence intensity in such a way that turbulence is suppressed in downdraft regions and enhanced in updraft regions as observed (LeMone 1976). As illustrated in Fig. 9 of LeMone et al. (2013) for the Bougeault and Lacarrère (BouLac), Mellor–Yamada–Janjić (MYJ), and quasi-normal scale elimination (QNSE) PBL schemes [all of which solve the turbulent kinetic energy (TKE) equation], the vertical gradient of virtual potential temperature $\partial\Theta_v/\partial z$ is more negative (unstable) in updraft regions than downdraft regions, resulting in a horizontal variation of the buoyancy generation of TKE in the same sense.

The M-CISCs introduce complications that we are ill-equipped to assess. For example, M-CISC thermodynamic and wind fields impact surface fluxes, complicating the interaction between the resolved physics and subgrid physics specified in the user-specified land surface and surface-layer parameterization schemes. The effects of M-CISCs become particularly dramatic when they produce clouds, as illustrated in Fig. 5, which shows fluxes from the Noah land surface model (Chen and Dudhia 2001; Ek et al. 2003) along a flight track near Beaumont, Kansas, during the International H₂O Project (IHOP_2002) field experiment (Weckwerth et al. 2004) for 20 June using WRF version 2.1.2. Where there are clouds, the net radiation (and hence the available energy) drops significantly, leading to greatly reduced sensible and latent heat fluxes. Although the direction of this change is reasonable from a physical point of view, no careful comparison against observations has been done.

Finally, the nonlinear interaction between M-CISCs and the PBL scheme changes with grid spacing. Going from mesoscales to the terra incognita, grid size affects thermal stability, which affects PBL and surface schemes as well as M-CISC development (LeMone et al. 2010,

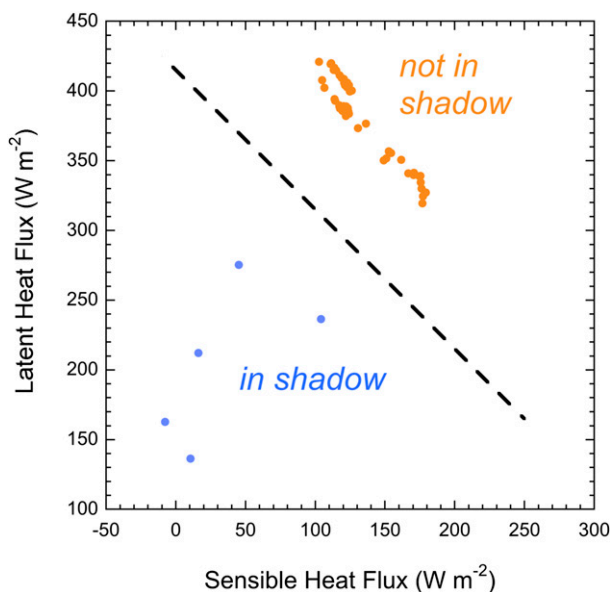


FIG. 5. For 20 Jun 2002 along the IHOP_2002 eastern flight track, surface fluxes along the eastern flight track for 1-km inner grid of WRF version 2.1 run with YSU PBL scheme. For further details, see LeMone et al. (2010).

2013). While M-CISCs grow rapidly at 1-km grid spacing for the three TKE-based PBL schemes used in LeMone et al. (2013), they still grow (but quite slowly) at 9-km spacing, resulting in a superadiabatic lapse rate (their Fig. 17). In contrast, the Yonsei University version 3.2 (YSU 3.2) scheme produces much weaker M-CISCs at 1 km, and a near-neutral lapse rate at 3 and 9 km. At 9-km resolution, the M-CISCs are too weak to mix the convective boundary layer (CBL), so the main mixing is by the BouLac, MYJ, and QNSE schemes themselves, while YSU 3.2 can mix the CBL without M-CISCs. However at 1-km grid mesh, all four schemes have near-neutral stratification (except for near the surface) when profiles are averaged horizontally; this is because the M-CISCs themselves are transporting heat from near the surface.

Why the difference between YSU and the TKE-based PBL schemes at $\Delta = 9$ km? The three TKE-based PBL schemes used here are based on the assumption of downgradient diffusion; that is, vertical fluxes are negatively proportional to the local vertical gradient. In contrast, the YSU 3.2 scheme adds nonlocal mixing through entrainment fluxes and fluxes that do not depend on the local vertical gradient. YSU 3.2 can produce near-neutral thermal stratification without M-CISCs, while the other schemes cannot.

It follows that the evolution of thermal stratification is different for the two types of scheme, as illustrated by the sequence of Θ_v profiles for MYJ and YSU 3.2 in Fig. 6. For MYJ (Fig. 6, top), the profiles start out with

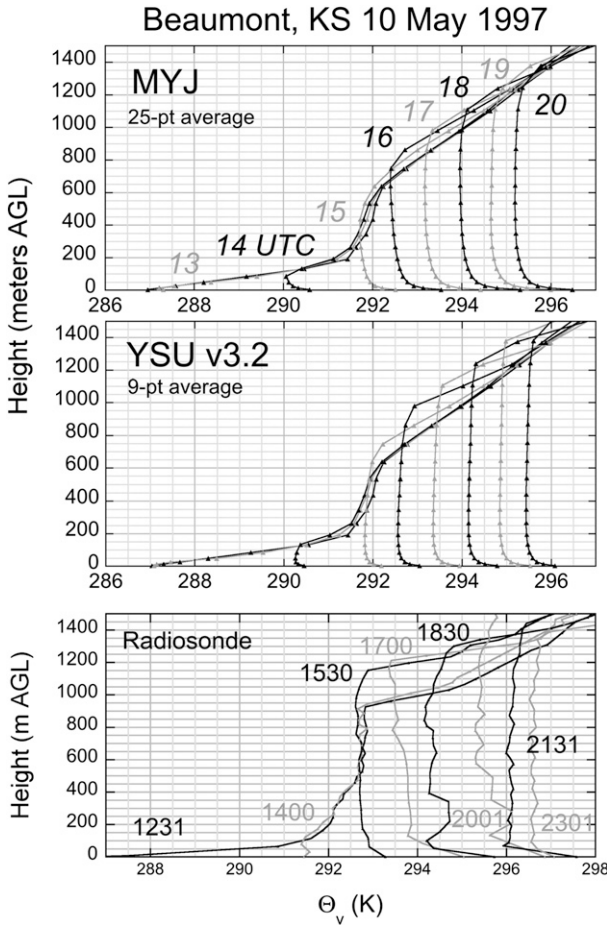


FIG. 6. For the 10 May 1997 case in LeMone et al. (2013), time sequences (UTC) of θ_v profiles at Beaumont. (top),(middle) For the commonly used MYJ TKE scheme and nonlocal YSU 3.2 scheme, respectively. Model soundings are horizontally averaged to remove the effects of CISCs, with the MYJ averaging scale larger because of stronger CISCs. (bottom) Time sequence of radiosonde soundings.

a superadiabatic lapse rate in the mid-PBL, but become neutral except for near the surface in the early afternoon as the M-CISCs form. On the other hand, for YSU 3.2, the profiles through the inner PBL remain neutral to stable (Fig. 6, middle). Similarly, the vigorous space-filling patterns in Fig. 3 are for the four PBL schemes that allow only local fluxes, leading to an accumulation of heat in the lower PBL, which grows the M-CISCs and which in turn drive the CBL to near neutrality. Conversely, the three schemes with only scattered PBL features all allow non-local transport.

3. Hypothesis

As the daytime-heating cycle begins, the ground temperature rises faster than that of the overlying atmosphere,

creating an intense near-surface superadiabatic layer. Ensuing turbulent motions transport heat upward, producing a well-mixed virtual potential temperature profile θ_v through the inner PBL. However, equilibrium profiles of θ_v typically retain a superadiabatic layer near the surface (Fig. 6; also Fig. 11.1 of Wyngaard 2010). It was shown in the previous section that superadiabatic lapse rates are common features of daytime fair-weather PBLs in WRF. Our hypothesis is that at current-day fine-grid resolutions, the typical mesoscale model reacts to the superadiabatic lapse rates by producing what appear to be “organized” PBL motions, that is, the M-CISCs, described above.

In the absence of viscosity or heat transfer, a layer of air in which θ_v decreases with height is unstable to infinitesimally small perturbations. For a general perturbation of the form $e^{i(kx+ly)} e^{\sigma t} \sin mz$, Rayleigh (1916) derives the following formula relating the growth rate σ to the scales of the perturbation represented by the respective wavenumbers $(k, l, m) = 2\pi(\lambda_x^{-1}, \lambda_y^{-1}, \lambda_z^{-1})$:

$$\sigma = \frac{\beta \sqrt{k^2 + l^2}}{\sqrt{k^2 + l^2 + m^2}}, \tag{3.1}$$

where

$$\beta^2 = -\frac{g}{\theta_{v0}} \frac{\partial \theta_{v0}}{\partial z} > 0 \tag{3.2}$$

and the other symbols have their usual meaning. For the case of a fluid bounded by impermeable horizontal plates at $z = 0$ and H , the fastest-growing modes occur with $\lambda_z = 2H$ and therefore we consider here only cases with $m = \pi/H$. With m so fixed, (3.1) implies that waves of the shortest horizontal wavelengths grow fastest (i.e., $\sigma \rightarrow \beta$ monotonically as $\sqrt{k^2 + l^2} \rightarrow \infty$). For simplicity we consider here the case where the perturbations are two dimensional ($l = 0$).

The typical surface-heated PBL parameterization produces a superadiabatic layer over some depth near the lower surface (Fig. 6; Fig. 7, black line). If one were to apply (3.1) to the flow in a mesoscale model simulation with a PBL-produced profile similar to that in Fig. 7, then two considerations immediately present themselves: First, there is a lower limit on the scale λ_x , since numerical models have finite resolution; and second, all mesoscale models include frictional processes. Considering first the finite resolution of a numerical model, it is instructive to rewrite (3.1) (with $l = 0$) in terms of length scales, namely,

$$\frac{\sigma}{\beta} = \frac{1}{\sqrt{1 + (\lambda_x/2H)^2}}. \tag{3.3}$$

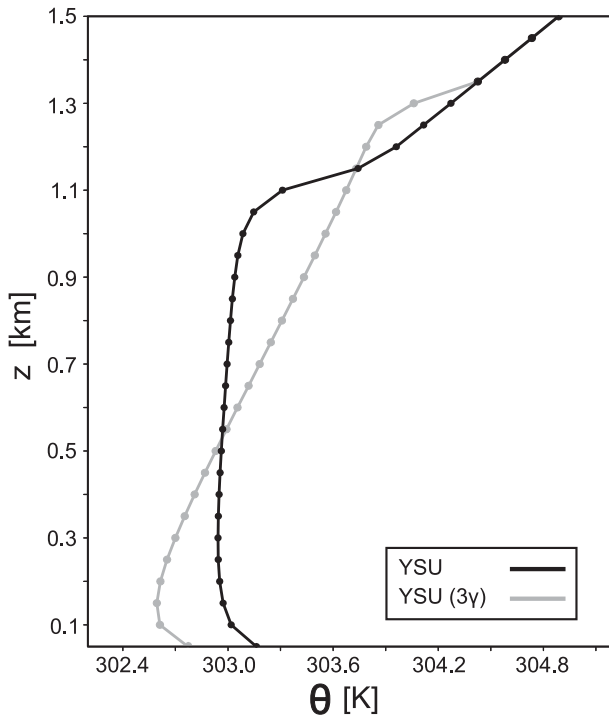


FIG. 7. Mean temperature profiles calculated with WRF using the YSU version 3.4 parameterization (black line) and a modified version that increases by a factor of 3 the countergradient term (gray line).

Here, (3.3) indicates that the fastest growth occurs when λ_x takes its minimum value. Identifying the depth of the superadiabatic layer with H and using an average constant lapse rate, we estimate from Fig. 7 that $\beta \approx 6 \times 10^{-5} \text{ s}^{-1}$ and $H \approx 300 \text{ m}$; considering that the minimum resolved scale is $\lambda_x \approx 8\Delta x$, a grid size of $\Delta x = 5000 \text{ m}$ ($\lambda_x/2H \approx 67$) would produce a growth rate of $\sigma \approx 9 \times 10^{-5} \text{ s}^{-1}$ (e -folding time $\tau \approx 3.1 \text{ h}$), while a grid size of $\Delta x = 500 \text{ m}$ ($\lambda_x/2H \approx 6.7$) would have $\sigma \approx 9 \times 10^{-4} \text{ s}^{-1}$ ($\tau \approx 0.31 \text{ h}$). The graph of (3.3) shown by the thin solid line in Fig. 8 illustrates this dependence. Hence, for the same unstable profile, one can expect to see small-scale, convectively unstable disturbances manifest themselves much sooner with the smaller grid interval, as shown in the previous section.

Second, mesoscale models are not inviscid. Including viscosity and heat conductivity in the stability analysis, Rayleigh (1916) shows that for boundaries with zero stress divergence, (3.1) can be generalized to his (37), which for the case where the coefficients of viscosity ν and heat transfer κ are equal gives

$$\frac{\sigma}{\beta} = \frac{1}{\sqrt{1 + (\lambda_x/2H)^2}} - \frac{\nu\pi^2}{\beta H^2} \left(1 + \frac{4H^2}{\lambda_x^2} \right). \quad (3.4)$$

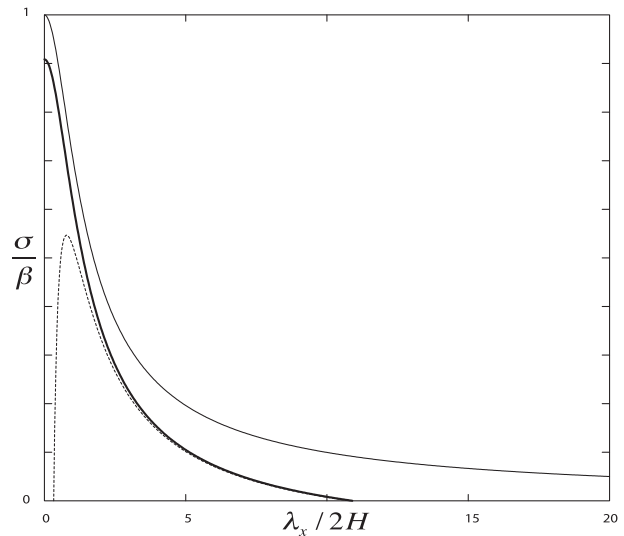


FIG. 8. Nondimensional growth rate vs nondimensional wavelength for the instability of a superadiabatic layer for inviscid, adiabatic flow (thin solid line); for viscous, adiabatic flow with $Ra = 1.16 \times 10^4$ (dotted line); and viscous, adiabatic flow with the same Ra , but with vertical diffusion only (thick solid line).

Rayleigh (1916, p. 440) observed from (3.4) that disturbances with either very long or very short wavelengths are stable and that therefore there exists a λ_x that gives the maximum growth rate for a given combination of β , ν , and H ; Rayleigh further found the maximum growth rate is zero (complete flow stability) when the Rayleigh number is

$$Ra = \frac{\beta^2 H^4}{\nu^2} < \frac{27\pi^4}{4} = 657.5. \quad (3.5)$$

Considering again the values for β and H given above, we estimate $Ra \approx 2.9 \times 10^4 \text{ m}^4 \text{ s}^{-2} / \nu^2$; a typical eddy viscosity $\nu \approx 5 \text{ m}^2 \text{ s}^{-1}$ gives $Ra = 1.16 \times 10^4$, indicating instability by (3.5). The thin dotted curve in Fig. 8 illustrates that diffusion produces both a shortwave and longwave cutoff to the instability.

Now in mesoscale models, a typical PBL parameterization produces an eddy viscosity $K(z)$ that acts only on vertical gradients of the predicted variables (e.g., Mellor and Yamada 1982; Pleim 2007; Hong et al. 2006; Nakanishi and Niino 2009).

Piotrowski et al. (2009) computed the marginal stability curve $\sigma(k, l, m; Ra) = 0$ for anisotropic diffusion ranging from all horizontal and no vertical diffusion to all vertical and no horizontal diffusion. The latter case is particularly relevant to this study, since it describes the basic anisotropic diffusion inherent in the typical PBL parameterization; in this case instead of (3.4), one obtains

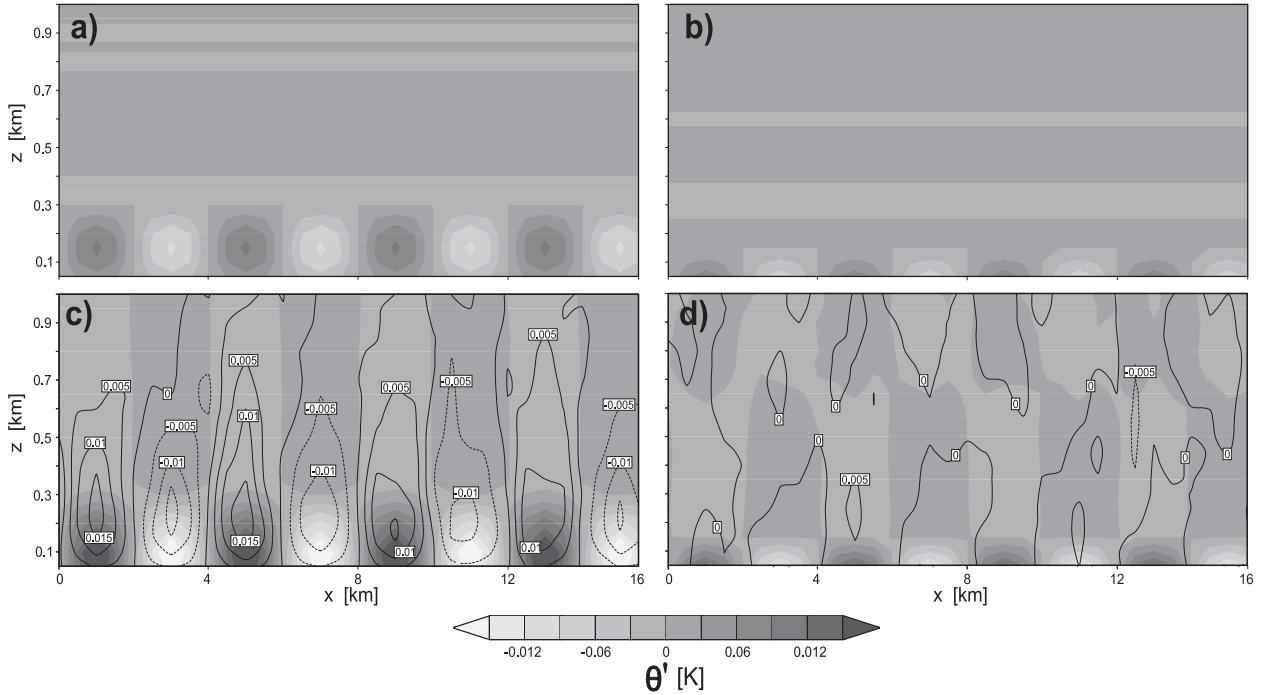


FIG. 9. Potential temperature perturbation (K, shaded) and vertical velocity (m s^{-1} , contours) at (top) $t = 0$ and (bottom) $t = 20$ min, (left) using the base-state potential temperature profile shown in Fig. 7 (the default YSU parameterization). (right) As in (left), but using a countergradient term 3 times larger than normal.

$$\frac{\sigma}{\beta} = \frac{1}{\sqrt{1 + (\lambda_x/2H)^2}} - \frac{\nu\pi^2}{\beta H^2} \quad (3.6)$$

for the growth rate. In contrast with (3.4), inspection of (3.6) reveals that there is no longer a shortwave cutoff but that the longwave cutoff is essentially unchanged and given by

$$\frac{\lambda_x^{\text{lwc}}}{2H} = \sqrt{\frac{\text{Ra}}{\pi^4} - 1}. \quad (3.7)$$

The heavy solid curve in Fig. 8 illustrates this behavior for the same parameter values as used above. In the example illustrated in Fig. 8 (thick solid curve), the loss of a shortwave cutoff in (3.6) would be irrelevant if that cutoff scale were less than the minimum resolved scale; however, one can see that going to yet higher resolutions with this anisotropic diffusion would allow for even greater growth rates.

To show that these considerations are relevant to the problem at hand, we have carried out several simulations of a growing convective boundary layer using WRF. The effects of turbulent motions are parameterized for the YSU PBL parameterization. Basically, the scheme represents turbulent fluxes using a downgradient diffusion with an additional nonlocal term to account for

countergradient transport in a way similar to that suggested by Troen and Mahrt (1986) that affects mainly the upper part of the PBL. We consider a two-dimensional flow with a domain length of 16 km and a height of 2 km. From the initial instant forward, the surface heat flux is set to 200 W m^{-2} . Starting from a stable potential temperature profile that increases by 6 K over the domain depth, the model is run for 2 h and develops the potential temperature profile shown in Fig. 7 (black line), which exhibits the classic growing mixed-layer shape; after 2 h of simulation the heat flux and the eddy viscosity are set to zero. Under these conditions, the temperature profile no longer changes through diffusive effects and any further evolution of the solution must come about through the horizontally inhomogeneous perturbations that we introduce at the 2-h end time of the heating.

For the first simulation, we let

$$\theta'(x, z, t = 2 \text{ h}) = 0.01 \sin(8\pi x/X) \sin(\pi z/H), \quad (3.8)$$

where $X = 16 \text{ km}$ and $H = 300 \text{ m}$, and where H is the height of the unstable layer; using 32 equally spaced horizontal grid points, we have $\Delta x = 500 \text{ m}$. Figure 9a shows a contour plot of (3.8), while Fig. 9c shows the solution $w(x, z, t)$ and $\theta'(x, z, t)$ after 20 min. The growth of convective eddies is evident through the obvious positive correlation of $w(x, z, t)$ and $\theta'(x, z, t)$. Repeating

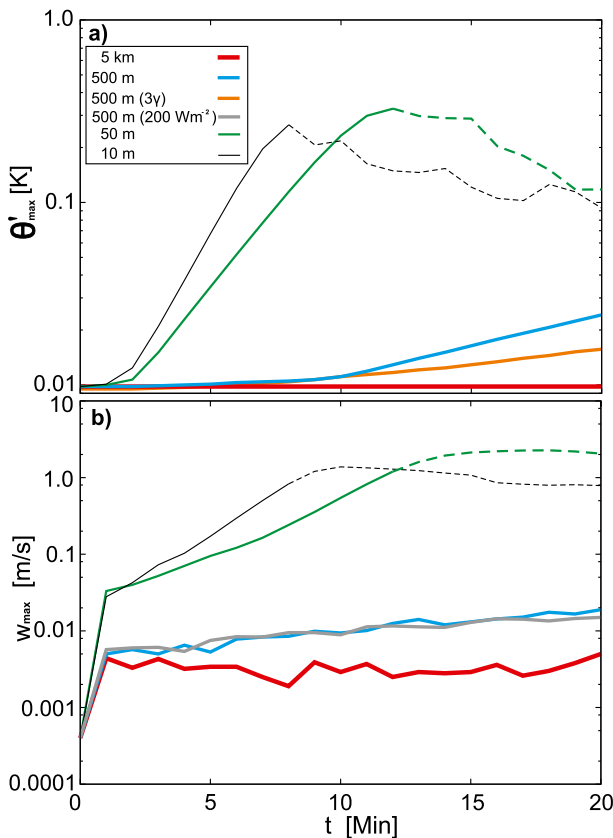


FIG. 10. Temporal evolution of (top) the maximum potential temperature perturbation and (bottom) w_{\max} . Results for different grid spacing and special cases are shown (see legend). The thin dashed lines indicate that the motion has reached nonlinear saturation and is outside the range of validity of the linear theory.

the same experiment with the same number of grid points in the x direction but with $X = 160$ km increases the horizontal grid spacing to $\Delta x = 5000$ m and significantly reduces the growth rate as shown in Figs. 10a,b, which present graphs of $\theta'_{\max}(t)$ and $w_{\max}(t)$, respectively, on a logarithmic scale for experiments with $\Delta x = 10, 50, 500$, and 5000 m. It is clear from Fig. 10 that permitting the model to resolve smaller scales allows increasing growth rates as predicted in Fig. 8. These instabilities saturate quickly (dashed lines in Fig. 10); on the other hand, the instability with $\Delta x = 500$ m grows to finite amplitude over a period of interest to the mesoscale modeler and has an easily recognizable scale (as in Fig. 2).

To make a somewhat closer connection with mesoscale simulations, we show in Fig. 10b the growth of $w_{\max}(t)$ for a case where the heat flux is maintained and the boundary layer continues to evolve (increasing in mean temperature and growing in depth, but otherwise maintaining its profile) over the period under study; clearly the growth of the instability is similar with (gray line) and without (blue line) the continued heating.

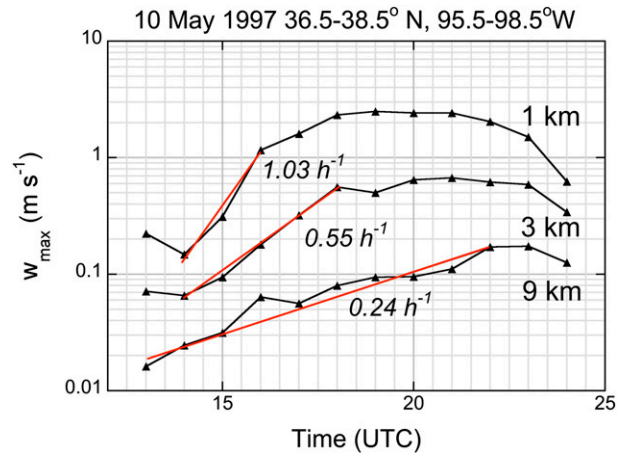


FIG. 11. For MYJ, maximum absolute value of w as a function of time for a domain centered over Beaumont for three simulations with $\Delta = 1, 3$, and 9 km and no feedback from smaller scales. Least squares best-fit lines correspond to the growth rates for each curve. Straight lines mark the time over which the growth rate was calculated.

Figures 9b,d and the orange curve in Fig. 10 show a simulation using the YSU scheme but with the non-local term (γ) arbitrarily increased by a factor of 3. As expected, the growth rate is reduced (but at the expense of producing a profile that is far from resembling CBL observations, gray line in Fig. 7).

Our final step is to apply the theory to the simulation of a well-documented fair-weather day. Figure 11 shows the evolution of the largest absolute value of the maximum vertical velocity in the PBL as a function of time for a $264 \text{ km} \times 222 \text{ km}$ domain roughly centered on Beaumont for WRF version 3.2 simulations of 10 May 1997 as a part of the study described in LeMone et al. (2013). In each case, the larger domains are not influenced by the nested domains. Consistent with the foregoing discussion, the amplitudes and growth rates of the simulated secondary circulations are larger with finer grid spacing. It is interesting to note that the structures stop growing after progressively shorter times for smaller grid spacing as in our idealized WRF experiments (Fig. 10). The maximum PBL vertical velocity depicted for 1-km grid resolution, at about 2.5 m s^{-1} , looks like a good indicator of the maximum vertical velocity at a given point: the vertical motion fields reveal fairly uniform structure over the domain; moreover, a quick sample of the literature shows examples of vertical motions in rolls of up to 1 m s^{-1} in the tower data reported in LeMone (1973), and large vertical velocity values appear in rolls sampled using aircraft data by Weckwerth et al. (1999, $1.5\text{--}2.5 \text{ m s}^{-1}$) and LeMone (1976, 1.5 m s^{-1}) as well as dual-Doppler radar analyses (up to 2 m s^{-1} , Kropfli and Kohn 1977).

To compare the M-CISC growth rates in Fig. 11 with the theoretical growth rates, we normalized the σ estimates by

replacing $\partial\theta_{v0}/\partial z$ in (3.2) for the normalizing factor β with $\Delta\theta_{v0}/H$ with H taken as the depth of the superadiabatic layer. Both quantities were obtained from hourly profiles at Beaumont. We used two methods to estimate $\Delta\theta_{v0}$ —namely, simply taking the difference between the values at the top and bottom of the superadiabatic layer, and taking the difference between the top and bottom values as defined by a best-fit straight line that roughly represents the equivalent linear superadiabatic layer.

The normalized growth rates for $\Delta = 9$ km in Fig. 11 are much smaller than those predicted by the inviscid (3.3) as would be expected based on the viscous (3.6). Based on an average $H = 0.9$ km from the corresponding hourly Beaumont profiles from 1400 to 2200 UTC (0800–1600 LST) and estimates of $\lambda_x \sim 18$ –45 km from the 1600 and 1800 UTC horizontal vertical velocity maps, $\sigma/\beta \sim 2H/\lambda_x \simeq 0.04$ –0.1. Average β values obtained from the two methods for the corresponding period are 0.0074 and 0.0062 s^{-1} , respectively, with a total range between 0.0056 and 0.0126 s^{-1} , the largest values being for 1400 UTC. The normalized growth rate from Fig. 11 is thus of the order of 0.01 (range 0.005–0.012). A similar calculation for a best-fit line to the growth rate for 1300–1700 UTC (0.44 h^{-1} , not shown in the figure) also yields ~ 0.01 (range 0.005–0.02). Rayleigh numbers at 1300 UTC, based on vertical averages of eddy vertical heat diffusivity K_H (assumed equal to the eddy viscosity K_M) through the depth H , exceed 10000 for both methods, and were $O(1000)$ afterward. For $\lambda_x = 18$ km, Ra for zero growth from (3.6) is 9800, indicating growth prior to but not after 1300 UTC. No growth is predicted for $\lambda_x = 45$ km.

Applying the same treatment to the $\Delta = 1$ km case, the normalized growth rate is 0.03, about a tenth for that from (3.3), based on $\lambda_x = 2.8$ km, $\beta = 0.01 \text{ s}^{-1}$, and $H = 358$ m. During the period of growth (red line in Fig. 11), $\text{Ra} \sim 900$; this value falls to ~ 250 after growth stops, based on data from 1800 to 2000 UTC, consistent with $\text{Ra} = 333$ required for growth from (3.6) and the more neutral thermal stratification resulting from vertical mixing by the M-CISCs.

Without question the instability described above and captured in mesoscale models represents a real physical process representing the conversion of the potential energy of the temperature profile to the kinetic energy of the unstable motions. *However, with limited resolution, energy exchanges between CISCs and smaller-scale turbulence are not represented and hence a distorted picture of the CISCs can emerge.* This deficiency is one of the consequences of the terra incognita described by Wyngaard (2004). Current-day mesoscale models have resolutions high enough to capture the instability, but not so high as to simulate the full range of turbulent interactions that determine the ultimate distribution of energy over spatial scales and hence the correct boundary layer structures.

4. Parameterization of CISCs in RANS models

In this section, we explore two approaches designed to suppress M-CISCs by reducing the effective Rayleigh number (3.5) to below its critical value while providing more accurate vertical fluxes. As explained by Wyngaard (2004, 2010), mesoscale models can either adopt ensemble-average or volume-average approaches to obtain unresolved fluxes. For grid spacing significantly larger than the turbulence integral scale, these two approaches are indistinguishable. But in the terra incognita, where the grid spacing is comparable to the integral scale, the difference is profound: volume-averaged fields can be turbulent, while ensemble-averaged fields must stay laminar. The approaches described here are examples of the latter, with the ensemble-averaging operator used to filter the RANS equations. This operator is independent of grid spacing. As a consequence, the turbulence closures discussed represent the effect of all PBL circulations, including those spanning several horizontal grid lengths. It is shown that this approach could represent a real gain in accuracy (for a given resolution) for PBLs over heterogeneous surfaces.

To provide some examples of how this might work in practice, we modify the BouLac (Bougeault and Lacarrère 1989) PBL closure scheme, chosen because its formulation for the eddy viscosity and thermal diffusivity is simple, making the modifications and testing easier. The BouLac scheme computes the vertical eddy viscosity and vertical thermal diffusivity as

$$K_{M_z} = C_K l_K \sqrt{\text{TKE}}$$

$$K_{H_z} = K_{M_z}, \tag{4.1}$$

where $C_K = 0.4$, and l_K is a length scale estimated from the local value of TKE and the vertical profile of potential temperature using a parcel method.

For this sensitivity study, we adopt as the reference case STANDARD, the standard configuration (recommended in WRF) with the eddy viscosity K_{M_x} and thermal diffusivity K_{H_x} in the horizontal direction estimated following the Smagorinsky approach based on the flow deformation as

$$K_{M_x} = C_s^2 (\Delta x)^2 \left[\left(\frac{\partial U}{\partial x} - \frac{\partial V}{\partial y} \right)^2 + \left(\frac{\partial U}{\partial x} + \frac{\partial V}{\partial y} \right)^2 \right]$$

$$K_{H_x} = 3K_{M_x} \tag{4.2}$$

with $C_s = 0.25$. Here U and V are the two horizontal components of the velocity, and Δx is the horizontal grid spacing.

The first approach (PR3D) is to limit Ra to below its critical value Ra_{cr} , by modifying the thermal diffusivity.

The horizontal eddy viscosity and thermal diffusivity in PR3D are set equal to their vertical values, that is, $K_{M_x} = K_{M_z}$ and, $K_{H_x} = K_{H_z}$. Considering that $K_H = \text{Pr}^{-1} K_M$, we fix the turbulent Prandtl number Pr to ensure that $\text{Ra} < \text{Ra}_{\text{cr}}$, without modifying the eddy diffusivity computed by the PBL scheme. This gives

$$\text{Pr} = \min\left(1, \text{Ra}_{\text{cr}} \frac{K_M^2}{\beta^2 H^4}\right). \quad (4.3)$$

The value of Ra_{cr} is estimated as a function of the height of the superadiabatic layer H , and the horizontal grid spacing Δx . Since the eddy viscosity and β vary with height, an average value over H has been used. Using (4.3) and imposing $\sigma/\beta = 0$ in (3.4), used because horizontal and vertical eddy viscosities are equal, gives:

$$\text{Ra}_{\text{cr}} = \frac{\pi^4}{\left(\frac{\lambda_x}{2H}\right)^4} \left[1 + \left(\frac{\lambda_x}{2H}\right)^2\right]^3. \quad (4.4)$$

The Ra_{cr} used is the minimum obtained spanning the range of possible values of $\lambda_x = n\Delta x$ with $n = 1, \text{NX}$ (NX is the total number of points in one direction, although in practice it suffices to check only up to values of λ_x of 10–15 km, since the M-CISCs are usually much smaller than this). The expected effect is to increase the efficiency of the vertical heat diffusion, and at the same time reduce the effect of super-adiabaticity, thus decreasing the generation of M-CISCs.

In the second approach (GAMMA), we examine the role of introducing the countergradient nonlocal term in the parameterization of the turbulent heat flux in the vertical direction in a dry atmosphere (no water vapor). Letting

$$\overline{w'\theta'} = -K_{H_z} \left(\frac{\partial\theta}{\partial z} - \gamma\right) \quad (4.5)$$

allows for vertical transport of heat upward without a superadiabatic lapse rate. Since the gamma term allows for transfer of heat out of the superadiabatic layer referred to in the previous section, (4.5) allows for altering the lapse rate and thus reduces the instability that causes M-CISCs. For this demonstration, the countergradient term is estimated following Troen and Mahrt (1986), that is,

$$\gamma = \frac{C(\overline{w'T'})_0}{w_* h} \quad (4.6)$$

$C = 10,$

where $(\overline{w'T'})_0$ is the surface temperature flux and h is PBL depth. Here, the Prandtl number is kept equal to 1

($K_{H_x} = K_{M_x}$), and in the horizontal, the coefficients are computed with the Smagorinsky equation (4.2).

The STANDARD, GAMMA, and PR3D options are examined for two idealized cases with homogeneous surface heat fluxes over flat terrain at 45°N. The first is characterized by $-h/L = 100$ (typical for convective cells) and the second by $-h/L = 10$ (typical for roll formation). These are the same cases simulated with LES in the next section. A small random perturbation is introduced in the initial field of potential temperature to investigate the stability of the solution. We tested these approaches for three grid spacings: 1 km, 500 m, and 250 m, well within the terra incognita.

Figure 12 illustrates the sensitivity to grid spacing for STANDARD. For $-h/L = 100$, the cellular M-CISCs appear, with strong vertical velocities at 1000, 500, and 250-m grid spacing (Figs. 12a,c,e). The M-CISCs become smaller and slightly more cellular with larger maximum vertical velocities with smaller grid spacing. For the $-h/L = 10$ case, STANDARD generates detectable roll M-CISCs only for the 500- and 250-m grid spacing, with maximum vertical velocity larger and roll spacing smaller at smaller grid spacing (Figs. 12b,d,f), showing significant differences from those produced by LES (section 5; Fig. 15). On the other hand, the fields produced by GAMMA and PR3D are homogeneous and do not show any M-CISCs (not shown). It is important to remember, that since we are looking for the ensemble average, the correct solution must not have any M-CISCs.

While these modified simulations can prevent M-CISCs, the associated potential temperature profiles do not always resemble observations or mean profiles produced by LES (Fig. 13). For example, the GAMMA 1000-m grid-spacing simulation produces a shallow (but strong) superadiabatic layer near the surface, but much like the idealized experiment (Fig. 7 with 3γ), it is far more stable than observed (e.g., Fig. 6) or simulated in the LES, both for $-h/L = 100$ and $-h/L = 10$. However, the profiles produced by PR3D at 500- and 250-m grid-spacing simulations look more like the observed and LES profiles.

The strength of applying these options is the ability to represent the influence of finescale heterogeneities in the surface fluxes on the resulting flow fields without the uncertainties introduced by M-CISCs. Thus, it is important that the RANS approaches proposed here do not filter circulations induced by land-use heterogeneities. For this reason a test has been done where two rectangular lakes are introduced in the domain to generate land-use heterogeneity.

For this test, we embed two lakes in a 25 km \times 25 km domain with the land surface corresponding to the WRF

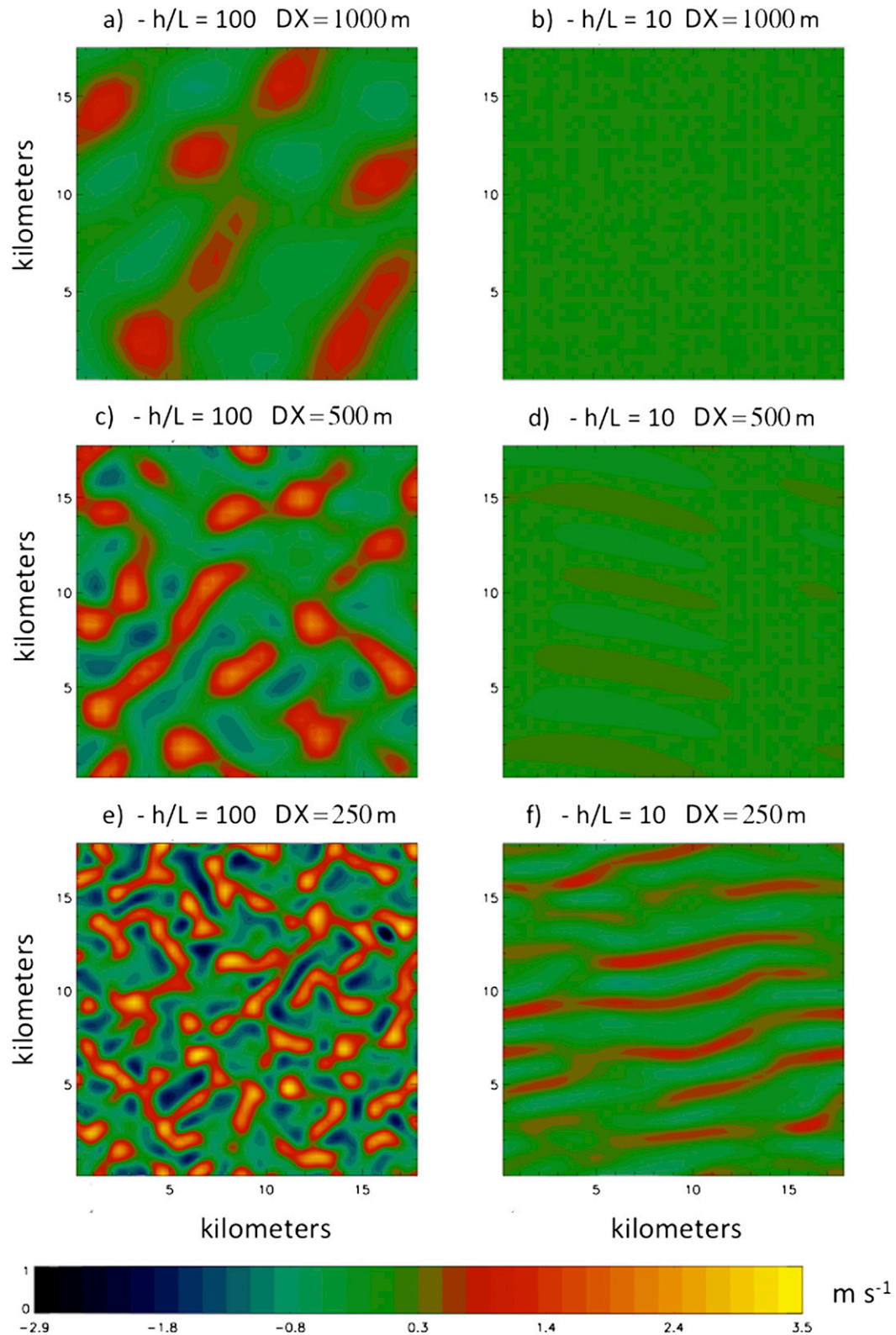


FIG. 12. Horizontal sections of vertical velocity, 400 m above ground, after 5.5 h of simulation, for grid spacing of (a),(b) 1000, (c),(d) 500, and (e),(f) 250 m for $-h/L =$ (left) 100 and (right) 10 for the STANDARD method.

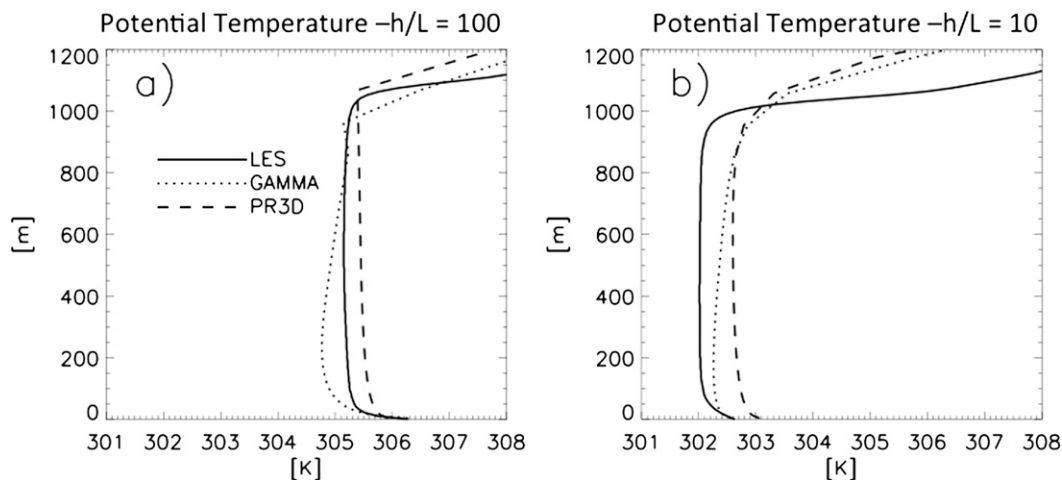


FIG. 13. Vertical profiles of potential temperature after 5.5 h of simulation for the GAMMA (dotted line) and PR3D (dashed line) simulations for the $-h/L =$ (a) 100 and (b) 10 cases at 1000-m grid spacing (results for 500- and 250-m grid spacing are equivalent). The solid line in both graphs represents the horizontal spatial average of the LES runs for the corresponding cases, which are assumed equivalent to the ensemble average.

category “dryland and cropland pasture.” A land surface model is used; conditions are for a clear-sky day at summer solstice (21 June), with initial wind of 3 m s^{-1} from the west (left in the figures). The simulation starts at 0900 LST and lasts for 9 h—the period with the strongest solar forcing. This ensures a strong surface heat flux (320 W m^{-2} maximum at 1300 LST). The lakes extend 2 km in the east–west direction and 5 km in the north–south direction, and they are separated by 2.5 km. The horizontal grid spacing is 250 m.

The local circulations induced by the lakes are expected to be of the scale of a few kilometers, comparable with the scale of the M-CISCs. Two runs are done, one with PR3D and one with STANDARD (Fig. 14). The PR3D simulation is able to reproduce the lake breezes (Fig. 14, right panels), while in the STANDARD simulation the M-CISCs destroy the lake-breeze signal (Fig. 14, left panels). *This comparison shows that the PR3D scheme is selective, in that it manages to eliminate the M-CISCs but still captures land–lake circulations at the same scale.*

It is important to remember that a RANS model seeks to reproduce the ensemble average rather than what would be actually observed at an instant in time; that is, the result is what would be observed with sufficient samples (aircraft passes, lidar scans) to “average out” the PBL eddies, or it is what would be modeled with an ensemble of LES runs with slightly different initial conditions. These ensemble fields are expected to respond only to the forcing induced by surface heterogeneities, and so they show horizontally homogeneous fields for the runs with homogeneous surface fluxes, and well-defined lake breezes for the lake cases.

The foregoing results show that STANDARD is inadequate for RANS simulations at subkilometer resolution not only because it produces M-CISCs that mask the effects of kilometer-scale surface heterogeneities but also because the M-CISCs are strongly resolution dependent. On the other hand, PR3D is capable of avoiding the formation of M-CISCs, thus effectively parameterizing the effect of the instabilities induced by super-adiabaticity, through a more correct representation of the vertical transport of heat, which is a necessary condition for RANS models. PR3D is a RANS approach, since it is not based on the size of the structure and not limited by the numerical resolution; thus, it has the potential to be applied safely even in the terra incognita for applications in which M-CISCs can introduce unwanted structure. The disadvantage is that it removes real and observable CISCs, since it only parameterizes their effects. A full quantitative evaluation of PR3D is beyond the scope of the present article, which aims only to indicate future ways of development. Preliminary results with quantitative comparisons against mean fields derived from LES simulations for idealized cases with heterogeneous surface fluxes have been presented in Martilli et al. (2014) and is the subject of ongoing work.

5. LES-based modeling

It has been shown that mesoscale simulations performed at coarse enough horizontal grid spacing ($\sim 10 \text{ km}$ or higher) do not produce M-CISCs. It is smaller grid spacings ($\sim 1 \text{ km}$) in conjunction with the near-surface superadiabatic lapse rate that lead to the

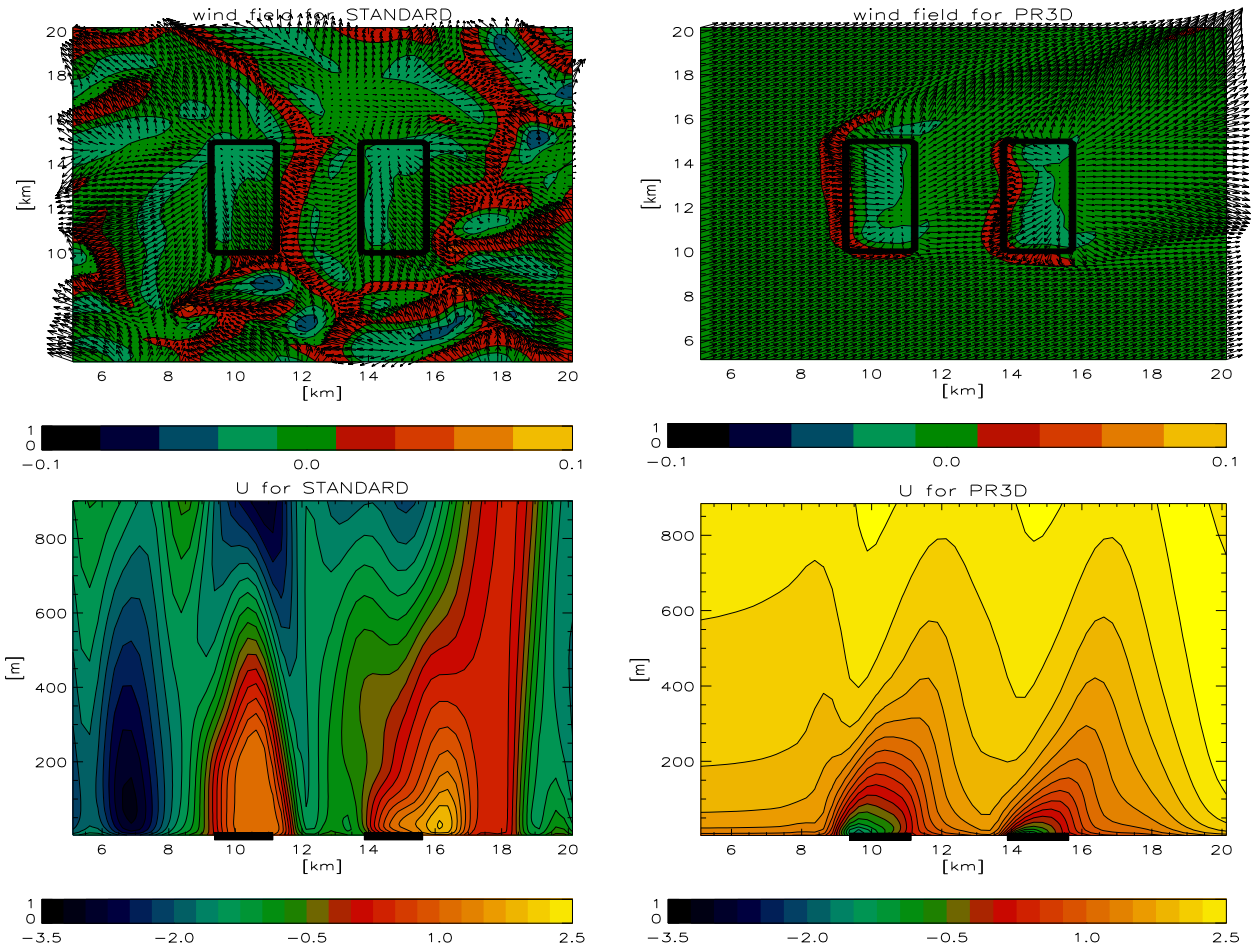


FIG. 14. Wind fields (arrows) and vertical velocities (colors) at the lowest model level for the (top) (left) STANDARD and (right) PR3D cases. The two lakes in the center of the domain are indicated by the black rectangles. Vertical sections through the middle of the lakes (west–east) of the U component of the wind are shown for the (bottom) (left) STANDARD and (right) PR3D cases. Black thick lines indicate the location of the two lakes in the center of the domain.

production of M-CISCs in the terra incognita. In this region, mesoscale models are able to generate structures associated with convection but are not able to represent the effects of energy exchange with smaller-scale turbulence, as LES simulations have been shown to do. In this section, we review and examine the capability of very fine-grid (~ 10 m) LES to illustrate their realism in simulating observed CISCs. We therefore analyze the simulated flow outside of the small-scale boundary of the terra incognita (Fig. 4).

Convective, neutrally stratified and stably stratified boundary layers have been studied extensively using LES. The first LES simulations of convective atmospheric boundary layers were carried out by Deardorff (1970), who was the first to use h/L to distinguish roll regimes from those with more random convective structure (Deardorff 1972). This work was followed by the use of the first LES with clouds (Sommeria 1976) to

replicate observations of rolls associated with tropical cloud streets (Sommeria and LeMone 1978), a case later simulated by Cuijpers and Duynkerke (1993) with finer grid spacing and a larger domain. Moeng and Sullivan (1994) used LES to contrast the roll and more convective regimes in greater detail, and Glendening (1996) conducted a study of roll dynamics using a large horizontal domain ($24.6 \text{ km} \times 18.4 \text{ km}$, $\Delta x = \Delta y = 64 \text{ m}$, $\Delta z = 32 \text{ m}$) to minimize the effects of roll distortion by periodic boundary conditions. De Roode et al. (2004) more generally addressed the question of the size of the numerical domain required in LES to resolve convective cells and rolls. Conzemius and Fedorovich (2008) studied the structures in the sheared convective PBL by combining observations from IHOP_2002 and LES.

For our current study, we performed several additional numerical experiments using LES to demonstrate how CISCs can be simulated in ideal cases for a variety

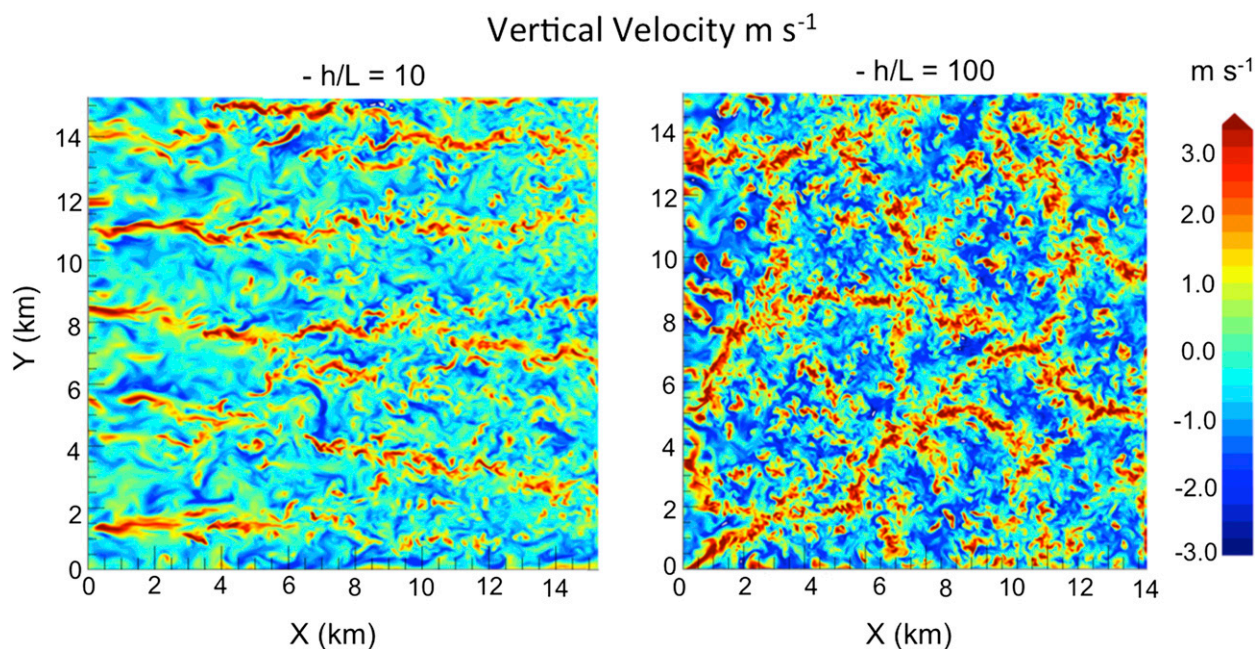


FIG. 15. Contours of vertical velocity on a horizontal plane ~ 400 m above the surface, for LES of a convective boundary layer with 30-m horizontal grid spacing: $-h/L =$ (left) 10 and (right) 100 corresponding to the convective roll regime and the convective cell regime, respectively.

of flow and stability conditions, using the LES version of WRF (Mirocha et al. 2010; Kirkil et al. 2012; Mirocha et al. 2013). There are two domains: the $18 \text{ km} \times 18 \text{ km}$ LES outer domain is resolved using $200 \times 200 \times 150$ grid cells with a $90 \text{ m} \times 90 \text{ m} \times 10 \text{ m}$ gridcell size with periodic boundary conditions on lateral boundaries, while the $\sim 15 \text{ km} \times 15 \text{ km}$ inner domain is resolved using $510 \times 510 \times 150$ grid cells with a $30 \text{ m} \times 30 \text{ m} \times 10 \text{ m}$ gridcell size. The inner domain gridcell size satisfies the LES convergence condition established by Sullivan and Patton (2011). The outer domain is used to provide boundary conditions with realistic turbulent inflow for the inner domain. The nesting is one way, so flow resolved in the inner domain does not affect the simulation in the outer domain. The outer domain partially insulates the simulated structures from the potentially unphysical effects of the periodic boundary conditions, such as being locked into a certain length scale or orientation.

We varied the surface sensible heat flux HFX and geostrophic forcing U_g to explore the combined effect of shear and buoyancy on the convective boundary layer structures. Following the foregoing discussion, we chose $-h/L = 10$ to simulate rolls and $-h/L = 100$ to simulate cellular convection. For the $-h/L = 10$ case, $U_g = 20 \text{ m s}^{-1}$ and $\text{HFX} = 100 \text{ W m}^{-2}$, while for $-h/L = 100$, $U_g = 5 \text{ m s}^{-1}$, and $\text{HFX} = 285 \text{ W m}^{-2}$. Surface moisture flux was set to zero. We first ran LES using only the outer domain for 4 h to spin up realistic turbulence and then

included the inner domain in our simulations. We then carried out nested LES with the two domains for an additional 2 h. Results presented here were obtained during the second hour of the nested simulation.

The vertical velocities in the inner domains are shown in Fig. 15 for the CISC roll case and cellular case. For both situations, the convective heating produced the expected superadiabatic near-surface temperature gradient (Fig. 13). Following theoretical expectations, M-CISCs, clearly seen from contours at 400 m ($h = 1 \text{ km}$), form in response to the superadiabatic condition. For the $-h/L = 10$ case, we observe five convective rolls across the width of our 15-km inner domain. In both cases, the vertical velocities are in the range expected from observations and other LES studies. While their average width is approximately 3 km, the rolls span the full 15 km in the along-wind direction. Since rolls can extend for hundreds of kilometers (see Fig. 1), our simulation has to be viewed as a sample of a roll field. Note that the smaller turbulent scales develop away (downwind) from the western (left) boundary, a consequence of turbulent cascade of energy. As these structures develop, the coherence of the convective rolls is reduced. When $-h/L = 100$, the LES produces cellular convective structure with characteristic horizontal length scales of a couple of kilometers in both directions.

Figure 16 shows the crosswind-direction vertical velocity spectra corresponding to the flows in Fig. 15,

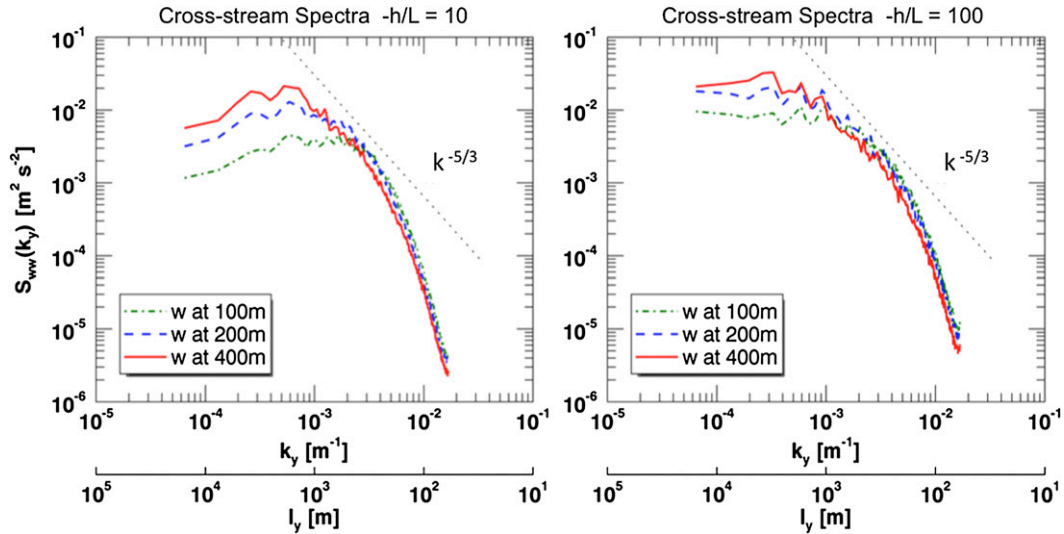


FIG. 16. For the vertical velocity fields in Fig. 15, rolls and cellular structure spectra computed in the y direction.

computed at 7500 m from the nested domain’s upwind (left) boundary. The LES produces a $k^{-5/3}$ slope over about a decade, before falling off rapidly, affording resolution of the CISCs as well as their associated turbulence. While the WRF mesoscale allows for energy exchange between the barely resolved M-CISCs and the resolved flow, the LES allows for energy exchange between M-CISCs and smaller-scale turbulence as well. These exchanges mostly drain energy away from the M-CISCs as illustrated in Bryan and Rotunno (2005), although the roll-turbulence exchange can also supply energy to the rolls (LeMone 1976).

The corresponding wavenumber-weighted spectra in Fig. 17 show a clear concentration of energy between 800 m and 2.5 km for the roll case, with a rapid falloff at longer wavelengths. There is more energy at longer wavelengths for the cell case. This is not surprising, given the appearance of the field at $x = 7.5$ km in Fig. 15, which shows significant vertical velocity along a line across half the domain. Inspection of the horizontal plots in Fig. 15 suggests an even more pronounced difference in the along-wind direction. Note the absence of a clear spectral gap between the M-CISCs and smaller turbulent scales. Although it can sometimes be quite obvious in crosswind observations (LeMone 1976, Fig. 3), it is often subtle to absent (Grossman 1982, Fig. 7), with the real differences showing up in along-wind spectra or spectra based on data at a small angle to the roll axis (LeMone 1973, Fig. 5).

Given that LES can represent CISCs and smaller scales, one can in principle use LES to develop a parameterization for use in the terra incognita of mesoscale models to correctly represent M-CISCs. Very

fine-resolution $O(10)$ m grid systems (Sullivan and Patton 2011) on domains of several tens or even a few hundreds of kilometers across would be needed to characterize the interactions involved in CISCs in order to develop such a parameterization. High-resolution grid systems would be needed, since the interactions of CISCs with smaller scales involve third-order terms (LeMone 1976, p. 1315). These simulations could be used to study the possibility of a closure that permits the development of M-CISCs with realistic flow of energy to and from smaller scales, as suggested by Wyngaard (2004).

The present discussion indicates that LES can reasonably simulate roll and cellular CISCs, and thus avoids

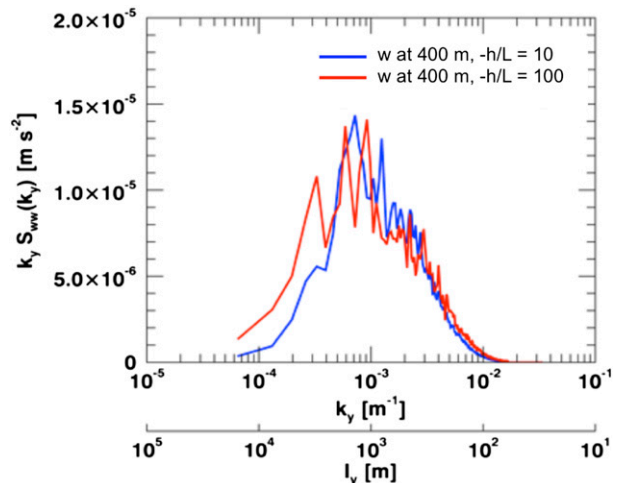


FIG. 17. As in Fig. 16, but for the 400-m data only, wavenumber-weighted spectra, plotted in log-linear coordinates so that the area under the curve is proportional to energy.

the problems associated with M-CISCs occurring with current mesoscale models in the terra incognita. Thus, LES can be used to improve PBL parameterizations in mesoscale models either to replicate CISCs better or, as done here, to eliminate M-CISCs by parameterizing the total PBL vertical fluxes. Some recent approaches include quantifying the fraction of turbulence resolved across the terra incognita as a function of h and Δx (Honnert et al. 2011; Shin and Hong 2013) or h and a diffusion length scale (Beare 2013), and representing turbulence through a statistical approach that emulates high-resolution LES modeling using conditional Markov chains and LES output (Dorrestijn et al. 2013).

6. Summary and discussion

In recent years, as computers have become more powerful, fine-grid [$O(1)$ km horizontally] numerical simulations are being performed using mesoscale models like WRF to investigate dispersion of pollutants, urban meteorology, the impacts of land surface heterogeneity, aspects of the boundary layer, the origin and evolution of convective precipitation, and hurricanes. Convectively induced secondary circulations (CISCs), typically less than 10 km across, are a common feature of the unstable PBL. While modeled CISCs (M-CISCs) are common and can look realistic, this paper has raised several questions regarding their reality, origins, and impact.

A mesoscale model run at high resolution presents a major problem with respect to M-CISCs in that they are grid-size dependent with respect to amplitude, horizontal size, and structure. In the present paper we have presented evidence that this problem is one of the consequences of modeling flows at grid spacings that are too small to justify the PBL schemes used and yet are too large for an explicit calculation of turbulent transfer; that is, these high-resolution mesoscale models are firmly within Wyngaard's (2004) terra incognita. For some PBL schemes and for grid meshes in the ~ 1 -km range, the wavelength and orientation of clouds produced by roll M-CISCs can be similar to those observed, and their vertical velocities are of the same order as observed. However, as the grid spacing becomes smaller, M-CISC patterns and their scale changes, and growth rates increase. M-CISCs locally modify virtual temperature, mixing ratio, and wind profiles in such a way that they share vertical transports with the PBL schemes.

We used the classical linear theory (Rayleigh 1916) to show that M-CISCs are the result of PBL parameterization-produced superadiabatic lapse rates. The classical theory also predicts the documented increase in growth rate

with smaller grid spacing. An idealized WRF simulation and a WRF simulation of an observed fair-weather boundary layer illustrate this dependence. In both, M-CISCs take over part of the vertical transport from the PBL scheme to make the virtual temperature profile more neutral and the Rayleigh number subcritical, after which growth slows down or ceases altogether. The theory thus explains why some PBL schemes [such as YSU and Mellor–Yamada–Nakanishi–Niino level 3 (MYNN3)] produce weaker M-CISCs, since their nonlocal transport terms make the potential temperature profile more nearly neutral and thus keeps the Rayleigh number near or below its critical value.

Guided by the theory, we explored some modifications to the BouLac PBL scheme to suppress the M-CISCs. The first approach sets horizontal eddy viscosity and eddy diffusivity to their vertical values and fixes the turbulent Prandtl Number (PR3D) so that the Rayleigh number remains subcritical, while the second approach introduces nonlocal transport (GAMMA) to the heat flux term to reduce the modeled superadiabatic lapse rates. The PR3D method successfully suppresses M-CISCs for horizontal grid spacing of 1 km, 500 m, and 250 m. The GAMMA experiment succeeded in M-CISC suppression at 1 km though at the expense of introducing artificial stability in the upper convective boundary layer through the nonlocal term.

If CISCs or their impact are the focus, then LES enables the resolution of CISCs and smaller scales. Resolution requirements for LES are not extremely restrictive, since we need only to resolve inertial range scales, which are several orders of magnitude larger (~ 10 m) than Kolmogorov microscales (~ 0.01 m), reducing the gridpoint requirements to less than 10^9 . A combination of a fine grid, large domain, and techniques to avoid the direct effect of periodic boundary conditions is a reasonable route to study CISCs and their interaction with smaller-scale turbulence. Given the capabilities of LES, a reasonable approach for accurate simulations that eliminate M-CISCs would be to compare results of PR3D, GAMMA, or similar simulations with LES-based statistics to find the optimum approach to minimizing the differences.

Improving representation of M-CISCs rather than removing them from mesoscale models may be desirable in some cases. For example, M-CISCs appear to improve forecasts of convective initiation as discussed by Kain et al. (2013) and roll CISCs have been observed to interact with cells in a squall line to produce tornado-bearing thunderstorms (Wakimoto and Wilson 1989). For such applications, it is recommended that improved PBL schemes be developed to correctly simulate M-CISCs, including their interaction with smaller scales,

following Wyngaard (2004). Further study is needed to identify the optimal combinations of resolution, PBL parameterization, and model diffusion for severe-weather forecast applications.

This paper has emphasized practical and theoretical problems with the present-day simulations of M-CISCs. We note that a similar and complementary treatment on this subject was submitted at about the same time (Zhou et al. 2014).

Acknowledgments. The lead author wishes to thank NCAR for its sponsorship and its interest in this study, and to thank its Faculty Fellowship Program of the Advanced Study Program (ASP) for providing him with on-site support. A. Martilli was supported by Project Supercomputation and E-Science (SyeC) from the CONSOLIDER Programme of Spanish Economy and Innovation Ministry.

REFERENCES

- Beare, R. J., 2013: A length scale defining partially-resolved boundary-layer turbulence simulations. *Bound.-Layer Meteor.*, **151**, 39–55, doi:10.1007/s10546-013-9881-3.
- Bornstein, R. D., E. Gutierrez, J. Gonzalez, A. Martilli, F. Chen, and J. K. Ching, 2012: Effect of sub-kilometer grid-spacing and time step magnitude on the formation of horizontal-vortices in urbanized-WRF simulations of NYC. *17th Conf. on Air Pollution Meteorology with the Air and Waste Management Association*, New Orleans, LA, Amer. Meteor. Soc., 6.6. [Available online at <https://ams.confex.com/ams/92Annual/webprogram/Paper199588.html>.]
- Bougeault, P., and P. Lacarrère, 1989: Parameterization of orography-induced turbulence in a mesobeta-scale model. *Mon. Wea. Rev.*, **117**, 1872–1890, doi:10.1175/1520-0493(1989)117<1872:POOITI>2.0.CO;2.
- Bryan, G., and R. Rotunno, 2005: Statistical convergence in simulated moist absolutely unstable layers. *11th Conf. on Mesoscale Processes*, Albuquerque, NM, Amer. Meteor. Soc., 1M.6. [Available online at https://ams.confex.com/ams/32Rad11Meso/techprogram/paper_96719.htm.]
- Byun, D. W., and K. L. Schere, 2006: Review of the governing equations, computational algorithms, and other components of the Models-3 Community Multiscale Air Quality (CMAQ) modeling system. *Appl. Mech. Rev.*, **59**, 51–77, doi:10.1115/1.2128636.
- Chen, F., and J. Dudhia, 2001: Coupling an advanced land surface–hydrology model with the Penn State–NCAR MM5 modeling system. Part I: Model implementation and sensitivity. *Mon. Wea. Rev.*, **129**, 569–585, doi:10.1175/1520-0493(2001)129<0569:CAALSH>2.0.CO;2.
- Conzemius, R. J., and E. Fedorovich, 2008: A case study of convective boundary layer development during IHOP_2002: Numerical simulations compared to observations. *Mon. Wea. Rev.*, **136**, 2305–2320, doi:10.1175/2007MWR2193.1.
- Cuijpers, J. W. M., and P. G. Duynkerke, 1993: Large eddy simulation of trade wind cumulus clouds. *J. Atmos. Sci.*, **50**, 3894–3908, doi:10.1175/1520-0469(1993)050<3894:LESOTW>2.0.CO;2.
- Deardorff, J. W., 1970: Preliminary results from numerical integrations of the unstable planetary boundary layer. *J. Atmos. Sci.*, **27**, 1209–1211, doi:10.1175/1520-0469(1970)027<1209:PRFNIO>2.0.CO;2.
- , 1972: Numerical investigations of neutral and unstable planetary boundary layers. *J. Atmos. Sci.*, **29**, 91–115, doi:10.1175/1520-0469(1972)029<0091:NIONAU>2.0.CO;2.
- De Roode, S. R., P. G. Duynkerke, and H. J. J. Jonker, 2004: Large-eddy simulation: How large is large enough? *J. Atmos. Sci.*, **61**, 403–421, doi:10.1175/1520-0469(2004)061<0403:LSHLIL>2.0.CO;2.
- Dorrestijn, J., D. T. Crommelin, A. P. Siebesma, and H. J. J. Jonkers, 2013: Statistical parameterization of shallow cumulus convection estimated from high-resolution model data. *Theor. Comput. Fluid Dyn.*, **27**, 133–148, doi:10.1007/s00162-012-0281-y.
- Ek, M. B., K. E. Mitchell, Y. Lin, E. Rogers, P. Grummann, V. Koren, G. Gayno, and J. D. Tarpley, 2003: Implementation of the Noah land-use model advances in the NCEP operational mesoscale Eta model. *J. Geophys. Res.*, **108**, 8851, doi:10.1029/2002JD003296.
- ESRL, 2006: By land, air, sea and satellite, NOAA seeks improved air quality and its links to climate. NOAA ESRL News. [Available online at <http://www.esrl.noaa.gov/news/2006/texaqs/>.]
- Glendening, J. W., 1996: Lineal eddy features under strong shear conditions. *J. Atmos. Sci.*, **53**, 3430–3449, doi:10.1175/1520-0469(1996)053<3430:LEFUSS>2.0.CO;2.
- Grossman, R. L., 1982: An analysis of vertical velocity spectra obtained in the BOMEX fair-weather, trade-wind boundary layer. *Bound.-Layer Meteor.*, **23**, 323–357, doi:10.1007/BF00121120.
- Hong, S.-Y., Y. Noh, and J. Dudhia, 2006: A new vertical diffusion package with an explicit treatment of entrainment processes. *Mon. Wea. Rev.*, **134**, 2318–2341, doi:10.1175/MWR3199.1.
- Honnert, R., V. Masson, and F. Couvreur, 2011: A diagnostic for evaluating the representation of turbulence in atmospheric models at kilometeric scale. *J. Atmos. Sci.*, **68**, 3112–3131, doi:10.1175/JAS-D-11-061.1.
- Kain, J. S., and Coauthors, 2013: A feasibility study for probabilistic convection initiation forecasts based on explicit numerical guidance. *Bull. Amer. Meteor. Soc.*, **94**, 1213–1225, doi:10.1175/BAMS-D-11-00264.1.
- Kirkil, G., J. D. Mirocha, E. Bou-Zeid, F. Katopodes Chow, and B. Kosović, 2012: Implementation and evaluation of dynamic subfilter-scale stress models for large-eddy simulation using WRF. *Mon. Wea. Rev.*, **140**, 266–284, doi:10.1175/MWR-D-11-00037.1.
- Kropfli, R. A., and N. M. Kohn, 1977: Persistent horizontal rolls in the urban mixing layer as revealed by dual Doppler radar. Preprints, *Sixth Conf. on Planned and Inadvertent Weather Modification*, Champaign–Urbana, IL, Amer. Meteor. Soc., 13–16.
- LeMone, M. A., 1973: The structure and dynamics of horizontal roll vortices in the planetary boundary layer. *J. Atmos. Sci.*, **30**, 1077–1091, doi:10.1175/1520-0469(1973)030<1077:TSADOH>2.0.CO;2.
- , 1976: Modulation of turbulent energy by longitudinal rolls in an unstable planetary boundary layer. *J. Atmos. Sci.*, **33**, 1308–1320, doi:10.1175/1520-0469(1976)033<1308:MOTEBL>2.0.CO;2.
- , F. Chen, M. Tewari, J. Dudhia, B. Geerts, Q. Miao, R. I. Coulter, and R. L. Grossman, 2010: Simulating the

- IHOP_2002 fair-weather CBL with the WRF-ARW-Noah modeling system. Part II: Structures from a few kilometers to 100 km across. *Mon. Wea. Rev.*, **138**, 745–764, doi:10.1175/2009MWR3004.1.
- , M. Tewari, F. Chen, and J. Dudhia, 2013: Objectively determined fair-weather CBL depths in the ARW-WRF model and their comparison to CASES-97 observation. *Mon. Wea. Rev.*, **141**, 30–54, doi:10.1175/MWR-D-12-00106.1.
- Martilli, A., R. Rotunno, J. Ching, and M. A. LeMone, 2014: A 3D RANS approach based on a modification of the effective Prandtl number for high resolution mesoscale simulations. *26th Conf. on Weather Analysis and Forecasting/22nd Conf. on Numerical Weather Prediction*, Atlanta, GA, Amer. Meteor. Soc., P614. [Available online at <https://ams.confex.com/ams/94Annual/webprogram/Paper233260.html>.]
- Mellor, G. L., and T. Yamada, 1982: Development of a turbulence closure model for geophysical fluid problems. *Rev. Geophys. Space Phys.*, **20**, 851–875, doi:10.1029/RG020i004p00851.
- Miao, S., and F. Chen, 2008: Formation of horizontal convective rolls in urban areas. *Atmos. Res.*, **89**, 298–304, doi:10.1016/j.atmosres.2008.02.013.
- Mirocha, J. D., J. K. Lundquist, and B. Kosović, 2010: Implementation of a nonlinear subfilter turbulence stress model for large-eddy simulation in the Advanced Research WRF Model. *Mon. Wea. Rev.*, **138**, 4212–4228, doi:10.1175/2010MWR3286.1.
- , G. Kirkil, E. Bou-Zeid, F. K. Chow, and B. Kosović, 2013: Transition and equilibration of neutral atmospheric boundary layer flow in one-way nested large-eddy simulations using the Weather Research and Forecasting Model. *Mon. Wea. Rev.*, **141**, 918–940, doi:10.1175/MWR-D-11-00263.1.
- Moeng, C.-H., and P. P. Sullivan, 1994: A comparison of shear- and buoyancy-driven planetary boundary layer flows. *J. Atmos. Sci.*, **51**, 999–1022, doi:10.1175/1520-0469(1994)051<0999:ACOSAB>2.0.CO;2.
- Nakanishi, N., and H. Niino, 2009: Development of an improved turbulence closure model for the atmospheric boundary layer. *J. Meteor. Soc. Japan*, **87**, 895–912, doi:10.2151/jmsj.87.895.
- Piotrowski, Z. P., P. K. Smolarkiewicz, S. P. Malinowski, and A. A. Wyszogrodzki, 2009: On the numerical realizability of thermal convection. *J. Comput. Phys.*, **228**, 6268–6290, doi:10.1016/j.jcp.2009.05.023.
- Pleim, J. E., 2007: A combined local and nonlocal closure model for the atmospheric boundary layer. Part I: model description and testing. *J. Appl. Meteor. Climatol.*, **46**, 1383–1395, doi:10.1175/JAM2539.1.
- Rayleigh, L., 1916: LIX. On convection currents in a horizontal layer of fluid, when the higher temperature is on the under side. *Philos. Mag.*, **32**, 529–546, doi:10.1080/14786441608635602.
- Shin, H. H., and S.-Y. Hong, 2013: Analysis of resolved and parameterized vertical transports in convective boundary layers at gray-zone resolutions. *J. Atmos. Sci.*, **70**, 3248–3260, doi:10.1175/JAS-D-12-0290.1.
- Skamarock, W. C., and Coauthors, 2008: A description of the Advanced Research WRF version 3. NCAR Tech. Note TN-475+STR, 113 pp. [Available online at http://www.mmm.ucar.edu/wrf/users/docs/arw_v3_bw.pdf.]
- Sommeria, G., 1976: Three-dimensional simulation of turbulent process in an undisturbed trade wind boundary layer. *J. Atmos. Sci.*, **33**, 216–241, doi:10.1175/1520-0469(1976)033<0216:TDSOTP>2.0.CO;2.
- , and M. A. LeMone, 1978: Direct testing of a three-dimensional model of the planetary boundary layer against experimental data. *J. Atmos. Sci.*, **35**, 25–39, doi:10.1175/1520-0469(1978)035<0025:DTOATD>2.0.CO;2.
- Sullivan, P. P., and E. G. Patton, 2011: The effect of mesh resolution on convective boundary layer statistics and structures generated by large-eddy simulation. *J. Atmos. Sci.*, **68**, 2395–2415, doi:10.1175/JAS-D-10-05010.1.
- Troen, I., and L. Mahrt, 1986: A simple model of the atmospheric boundary layer: Sensitivity to surface evaporation. *Bound.-Layer Meteor.*, **37**, 129–148, doi:10.1007/BF00122760.
- UCAR, 2014: ARW version 3 modeling system user's guide. UCAR Doc., 423 pp. [Available online at http://www2.mmm.ucar.edu/wrf/users/docs/user_guide_V3/ARWUsersGuideV3.pdf.]
- Wakimoto, R. M., and J. W. Wilson, 1989: Non-supercell tornadoes. *Mon. Wea. Rev.*, **117**, 1113–1140, doi:10.1175/1520-0493(1989)117<1113:NST>2.0.CO;2.
- Weckwerth, T. M., J. W. Wilson, R. M. Wakimoto, and N. A. Crook, 1997: Horizontal convective rolls: Determining the environmental conditions supporting their existence and characteristics. *Mon. Wea. Rev.*, **125**, 505–526, doi:10.1175/1520-0493(1997)125<0505:HCRDTE>2.0.CO;2.
- , T. W. Horst, and J. W. Wilson, 1999: An observational study of the evolution of horizontal convective rolls. *Mon. Wea. Rev.*, **127**, 2160–2179, doi:10.1175/1520-0493(1999)127<2160:AOSOTE>2.0.CO;2.
- , and Coauthors, 2004: An overview of the International H2O Project (IHOP_2002) and some preliminary highlights. *Bull. Amer. Meteor. Soc.*, **85**, 253–277, doi:10.1175/BAMS-85-2-253.
- Wyngaard, J. C., 2004: Towards numerical modeling in the “terra incognita.” *J. Atmos. Sci.*, **61**, 1816–1826, doi:10.1175/1520-0469(2004)061<1816:TNMITT>2.0.CO;2.
- , 2010: *Turbulence in the Atmosphere*. Cambridge University Press, 393 pp.
- Xue, M., and W. J. Martin, 2006: A high-resolution modeling study of the 24 May 2002 dryline case during IHOP. Part I: Numerical simulation and general evolution of the dryline and convection. *Mon. Wea. Rev.*, **134**, 149–171, doi:10.1175/MWR3071.1.
- Young, G. S., D. A. R. Kristovich, M. R. Hjelmfelt, and R. C. Foster, 2002: Rolls, streets, waves, and more: A review of quasi-two-dimensional structures in the atmospheric boundary layer. *Bull. Amer. Meteor. Soc.*, **83**, 997–1001, doi:10.1175/1520-0477(2002)083<0997:RSWAMA>2.3.CO;2.
- Zhou, B., J. S. Simon, and F. K. Chow, 2014: The convective boundary layer in the terra incognita. *J. Atmos. Sci.*, **71**, 2545–2563, doi:10.1175/JAS-D-13-0356.1.